Proceedings of ASME Turbo Expo 2011
GT2011
June 6-10, 2011, Vancouver, British Columbia, Canada

GT2011-46560

A PRELIMINARY NUMERICAL CFD ANALYSIS OF TRANSONIC COMPRESSOR ROTORS WHEN SUBJECTED TO INLET SWIRL DISTORTION

Javier Castaneda, Ahad Mehdi, Domenico di Cugno, Vassilios Pachidis
Department of Power and Propulsion
School of Engineering
Cranfield University, MK43 0AL, UK
Email: a.mehdi@cranfield.ac.uk

ABSTRACT

A preliminary investigation of a CFD capability to assess the impact of inlet swirl distortion on transonic compressor rotors has been carried out. In the late 1960s with the advent of turbo fan engines, industry and government agencies became increasingly aware of the inlet total pressure distortion problem. Since then, the inlet/engine compatibility assessment has become a significant issue within the propulsion system life cycle. Nowadays the development of high-performance military aircraft and UAV with maneuvers before unthinkable, entail considerable levels of inlet flow angularity. The importance of developing a rigorous methodology to understand the effect of inlet swirl distortion on turbomachinery has also become one of the major concerns of present day.

NASA rotor 67 and 37 were selected for this investigation having different hub to tip radius and aspect ratios. The steady state CFD simulations were carried out on two types of inlet swirl distortion scenarios: Bulk swirl (both Rotor 37 and 67) and Ground vortex (only Rotor 67). A parametric study to define the swirl angle distribution for ground vortex cases was also accomplished. The non-dimensional ground clearance, wind conditions and core vortex location at the inlet/engine AIP were the parameters taken into account.

The study carried out suggests that ground vortex core location and vortex rotational direction greatly affect the shift of the speedline. This emphasizes the importance of identifying the radial location of ingested vortex core at the AIP as the turbomachinery response differs depending on it. Similar shift in speedlines for the bulk swirl cases were also observed.

NOMENCLATURE

A	Area
AIP	Aerodynamic Interface Plane
c	Constant
CEL	CFX Expression Language
CFD	Computational Fluid Dynamics
D	Diameter
h	Inlet height from the ground
LE	Leading Edge
n	Shape factor
O	Origin of global coordinate system
P	Total pressure
r	Radius
TE	Trailing Edge
U	Axial component of the velocity vector
V	Velocity component
α	Absolute angle
υ	Kinematic viscosity of the air
ξ	Circumferential cosine director
θ	Angular position
Γ	Circulation
x,y	Cartesian coordinates

Subscripts and superscripts

amb	Ambient conditions
c	Vortex core
in	Intake
l	Intake highlight
x	Axial direction
r	Radial direction
∞	Conditions far upstream
θ	Circumferential direction
‘	Local coordinate system
p	Generic point at inlet face
v	Vortex center

INTRODUCTION

Inlet flow distortion may be defined as the presence of a spatial or temporal deviation from uniform, steady, one-dimensional flow at the inlet/engine AIP. The introduction of non-axisymmetric flow can severely alter the compressor operation. The most common type of inlet flow distortion is total pressure distortion which was extensively summarized and reported by the SAE S16 committee **[1]**. With the advent of fighter aircraft fitted with very complex inlet shapes, the SAE S16 committee has shifted its attention to a new type of inlet flow distortion. The presence of a certain level of flow angularity at the compressor face has gained importance in recent time as the necessity to reduce radar detection has provoked inlets to become stealthier. Furthermore, the current tendency of increasing the bypass ratio in an effort to reduce noise and the engine specific fuel consumption has resulted in a greater likelihood of ground vortex formation. Unfortunately, total pressure distortion cannot be 2qso easily decoupled from this scenario. In general, total pressure and swirl distortion appear as a single problem, interacting in a nonlinear fashion **[2]**.

The influences on engine performance due to inlet flow distortion ranges from mechanical issues, such as blade resonance, to operability issues, such as limitations on transient performance. The latter restriction is mainly due to the loss in stability pressure ratio which occurs when distortion is present at the engine face. In fact, as presented in Table 1, it can be noticed that the surge margin loss associated with distortion effects can be the highest within the list; although actual values for surge margin impact of inlet distortion vary substantially.

Item	Percent compressor surge margin used
Control-system performance	1.0
Engine/engine scatter	1.0
Deterioration	0.5
Acceleration	4.0
Reynolds number	2.0
Power off-take	2.5
Intake Distortion	4.5
Remaining surge margin	3.0

Table 1. Possible surge margin engine specification [3].

To envisage compressor map tendencies when the compression system is subjected to inlet swirl distortion, the rotor blade row of both NASA Rotor 67 and NASA Rotor 37 were simulated by using steady state CFD. In order to individually examine the effect of swirl distortion on the turbomachinery, it was decided to decouple the distortion pattern with that of total pressure distortion. In this way these two different distortion patterns can be studied in detail separately without imposing any effect on each other and will be coupled once considerable research and knowledge in swirl distortion have been found. In this paper, first of all the geometries and standard numerical approach is outlined. Then, a particular emphasis is given to the methodology developed to model the inflow distorted distributions: pure bulk swirl and ground vortex. And finally, the validation of the CFD capability is presented.

GEOMETRIES INVESTIGATED

Rotor 37

Rotor 37 was designed in the seventies as part of an 8-stage compression system with a pressure ratio of 20:1. It was tested at the Lewis Research Centre, NASA **[4]**. The blade row is composed of 36 multiple-circular-arc blades, with a design total pressure ratio of 2.106 at a mass flow of 20.19kg/s. However, the two most studied points within the 100% speedline have been the near-peak efficiency point and the near-stall point. These points are associated with a mass flow of 98% and 92.5% of the choked mass flow, this being 20.93 kg/s. The main characteristics of the geometry and flowfield are shown in Table 2. The geometry and the designation of the stations which has been followed are shown in Fig. 1.

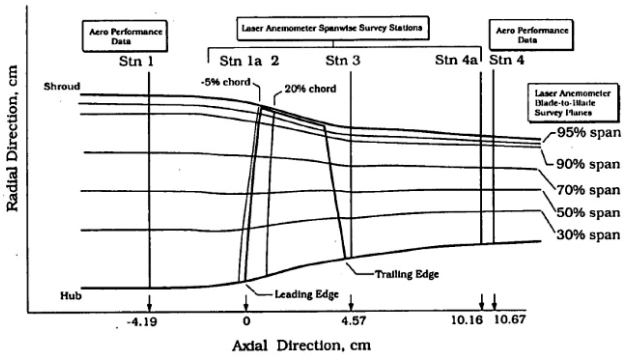

Figure 1. Rotor 37: Geometry definition including stations [5].

Rotor 67

The geometry of Rotor 67 corresponds to the first stage rotor of a two-stage transonic rotor designed and tested at the Lewis Research Center. Aerodynamic probe and laser anemometer measurements were utilised to take extensive data along the 100% speedline **[6]**. Table 2 contains the main specifications of the geometry and flow field. The real rotor geometry and the designation of the stations where the experimental data was collected are illustrated in Fig. 2.

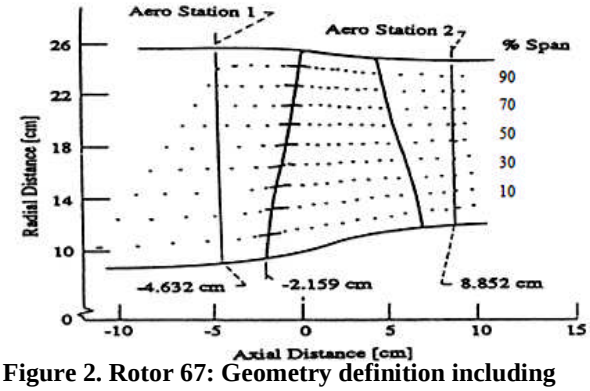

Figure 2. Rotor 67: Geometry definition including stations [7].

Similar to Rotor 37 the flow field is characterised by a shock wave system in combination with shredded tip leakage vortex. The low momentum region near the tip gap causes this tip leakage vortex to propagate and interact with the shock wave system especially near stall conditions, which resultantly causes the rotor to stall/surge. The complexity added to this rotor is the lower hub to tip radius ratios which makes the difference between the hub and shroud operating conditions even more noticeable.

Specification	NASA Rotor 37	NASA Rotor 67
Number of rotor blades	36	22
Rotational speed [RPM]	17188.7	16043
Choked mass flow [kg/s]	20.93	34.96
Total Pressure ratio(DP)	2.106	1.63
Rotor tip speed [m/s]	454.14	429
Tip clearance [cm]	0.04	0.061
Inlet tip relative Mach Number	1.48	1.38
Rotor aspect ratio	1.19	1.56
Hub to tip radius ratio	0.7	0.425

Table 2. Main specifications of the two rotors modelled [8].

COMPUTATIONAL APPROACH

Geometry

A number of geometry improvements were done to the original geometry provided by the corresponding NASA reports in order to carry out the consequent analysis.

1. Blade generation: Six blade sections along the span for Rotor 37 and fourteen for Rotor 67 were defined in order to allow the depiction of the stagger angle change in the spanwise direction.
2. LE and TE definition: The definition of the leading and trailing edge was improved by defining 24 points over these regions.
3. Shroud and Hub: The flow domain was extended in the axial direction at the inlet and outlet. However, the radius was maintained to be a constant. In extending both domain limits, it was expected to improve the convergence as the rotating blade is further away from the imposition of the boundary conditions.

The length scale of inlet flow distortion is considered to be the mean radius of the compression system. Hence, the flow domain was considerably extended for the simulations regarding distorted cases **[9]**. The approach adopted was to extend the outlet block a distance of 1.5 diameters in an attempt to allow the flow to be partially mixed before reaching the boundary condition at the back. This helps in better mixing of flow before it leaves the outlet. Especially in swirl distortion cases, the non-uniform flow fields at rotor exit are allowed to mix together, which considerably helps in CFD convergence time. Fig. 3 shows the outline of the flow domains of each rotor geometry.

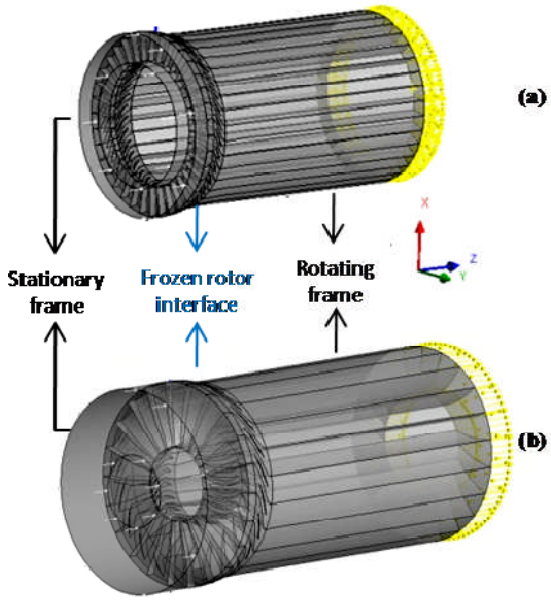

Figure 3. Flow domains: a) Rotor 37 b) Rotor 67.

Meshing Strategy

Once the geometry creation is finished, the mesh can be generated. A structured mesh with an H/C/J/L topology was found to be the one resulting in a better mesh quality. In this way, an H-type grid is defined at the inlet and outlet regions and a J-type extends along the flow passage. Moreover, around the blade an O-type grid was defined in order to better resolve the boundary layer. Although having reached an acceptable value of the skewness, regarding both the minimum and maximum face angles, the mesh was further improved. The skewness was able to be confined between the range (40-148) degrees, which is very close to the ideal range suggested by **[10]:** (45-145) degrees. The result of the meshing process is shown in Fig. 4.

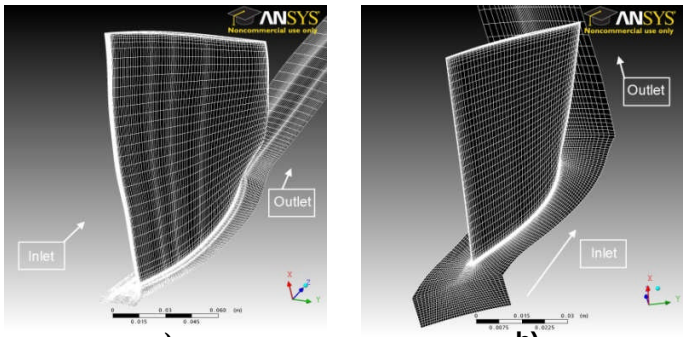

a) b)

Figure 4. View of the mesh over the blade: a) Rotor 67 b) Rotor 37.

The last aspect of the mesh concerns the boundary layer definition. Two different turbulence models were investigated; namely, K-epsilon and K-omega models. After performing some grid dependency simulations and taking in to account the accuracy required by the model and computational resources needed, it was decided use K-epsilon with scalable wall functions. The dimensionless wall distance (y^+) was fixed at a value of 50. However, the well-known underestimation of the efficiency has been reported to be partly due to very thick boundary layer **[11, 23]**. To reduce the boundary layer thickness and lower the recirculation, a lower value of y^+ was also implemented, thus taking a value of 25. The number of nodes within the boundary layer, having in mind that full-annulus simulations were going to be run, was chosen to be 11.

Flow solver and type of simulation

The CFD software selected to carry out the numerical simulations was ANSYS CFX, well-known because of its suitability to model turbomachinery flows. The meshes concerning the two rotor blades were produced via Turbogrid and Gambit.

Steady state simulations were selected against unsteady ones. Note that unsteady effects become dominant as the near-stall point is reached, but below this point they are contained within a range of low values **[9]**. Also as this is just a preliminarily CFD study, the unsteady effects near-stall point is beyond the scope of this paper. Thus, by performing steady simulations the main goal was to first understand the global effect of swirl distortion on turbomachinery, still a poorly understood research area. Full-annulus simulations were restricted to non-axisymmetric flows, namely, ground vortices cases. Therefore, as pure bulk swirl does not alter the symmetry of the flow field, a one-flow passage simulation was considered reasonable.

With reference to convergence criterion, the recommended value of RMS residuals for engineering applications is fixed to be 1E-05. Nevertheless, it was observed that the level of local imbalances decreased sharply once a good initial guess was obtained. In this way, the level of residuals reached at least a value of 1E-06. However, convergence cannot only be judged by means of level of residuals. A vital aspect of the simulation to claim its convergence is to have an unchanging value of the flow variables. For this purpose, the value of the mass flow at the exit of the domain and the total pressure of a point close to this boundary were monitored. So, the convergence criterion required to have falling residuals plus a constant value of the flow variables.

Clean boundary conditions

Total pressure and total temperature fields were imposed at the inlet. Table 3 shows the value of these variables, although it can be inferred that they correspond to atmospheric values. At the exit, the static pressure was used and also a non-slip condition was applied to all the metal elements. This combination of boundary conditions results in a robust procedure, although being sensitive to initial guess. In fact, the first simulations were the toughest to converge due to the "cold start" the simulation had to go through. Nonetheless, once the first simulation was totally converged, this was used as an initial condition for the following ones improving considerably the computational time. The method of producing the whole speedline was by means of increasing the static pressure at the outlet, which has the effect of throttling the compression system. The speedline calculated corresponds to a value of 100% of the design rotational speed.

Boundary conditions	NASA Rotor 37	NASA Rotor 67
Inlet total pressure [Pa]	101325	101325
Inlet total temperature [K]	288.15	288.15
Inlet turbulence intensity	3%	3%
Rotational speed [RPM]	17188.7	16043
Outlet static pressure [Pa]	Variable	Variable

Table 3. Boundary conditions specification for both rotor geometries.

Validation Study

A number of different meshes were created in order to carry out a mesh sensitivity analysis. Table 4 summarizes the main parameters of all the meshes used for Rotor 37 and Table 5 corresponds to the analysis with respect to Rotor 67.

Mesh	Nodes($1E^{+6}$)	Tip gap nodes
Coarse	4.5	0
Medium	11	0
Fine	19	0
Medium (lower y^+)	11	0
Hi-fi	24.2	0
Medium_clearance	11	10
Very fine	22	14

Table 4. Grid dependency study for Rotor 37.

Mesh	Nodes($1E^{+6}$)	Tip gap nodes
Coarse	5.8	0
Medium	12	0
Fine	19	0
Medium (lower y^+)	12	0
Hi-fi	36.8	0
Medium_clearance	12	8
Very fine	36.8	10

Table 5. Grid dependency study for Rotor 67.

From the previously presented tables, it can be observed that the tip clearance has not been fitted for all the meshes. The main reason of simulating distorted cases without tip gap is the fact that steady simulations were. The tip gap does not greatly affect the global performance of a rotor near design conditions, thus it will just increase the computational resources needed. However, it will play a vital role in unsteady simulations especially when predicting stalling under distorted conditions, and is under consideration for near future. The specification of the tip clearance gap for some clean cases considered a vena contracta effect following the suggestion of several researchers **[11,12,13].**

INFLOW DISTORTED BOUNDARY CONDITIONS

As an inlet boundary condition, the total pressure or flow direction can be prescribed to be constant or to follow a certain pattern. Therefore CEL expressions were used in CFX in order to prescribe non-uniform boundary conditions using analytical expressions.

Bulk Swirl

In this case, a certain flow direction was given to the flow at the inlet. To impose such flow angularity, the cosine directors of the velocity vector were calculated neglecting the radial component as suggested by previous researchers **[2,14]**. In Eq. (1-5), the simplicity of the formulae can be observed. The value of the axial velocity for the case of pure bulk swirl does not really matter since the restriction concerns only to the angle between the axial and the circumferential component.

$$V_x = c\left[\mathrm{m/s}\right] \tag{1}$$

$$V_\theta = V_x \mathrm{atan}\left(\frac{\alpha\pi}{180}\right) \tag{2}$$

$$\|V\| = \sqrt{V_x^2 + V_\theta^2} \tag{3}$$

$$\mu = \frac{V_x}{\|V\|} \tag{4}$$

$$\xi = \frac{V_\theta}{\|V\|} \tag{5}$$

Ground vortex

The main purpose of the analysis carried out by **[15]** was the development of a method to describe the swirl pattern produced by a ground vortex. Wind tunnel tests of a $1/30^{th}$ scale model intake were carried out to investigate the conditions at which the three types of ground vortex are formed, which are Quiescent, Headwind and Crosswind condition. SPIV (Stereoscopic Particle Image Velocimetry) and total pressure measurements enabled a thorough investigation of the flow field. The possibility of imposing as a boundary condition the vortex structure is quite attractive. For CFD purposes this allows modelling only the turbomachinery instead of having to simulate the ground as well. In this way, an empirical model to predict the vortex strength depending on the environment in which the engine is operated was established.

Just to clarify that the findings in which the method is based on will not be explained. The full explanation of the experimental data from which the method was built can be found in **[15].** The key parameters for defining the features of a ground vortex are the velocity ratio (U_i/U_∞) and the non-dimensional intake height, (h/D_i) this being the inputs to calculate vortex circulation.

The methodology cannot only consider the vortex model and the value of circulation, but also the direction and number of vortices characteristic of each vortex mechanism. In order to take into account the topology of the flow field for each vortex configuration, vortex visualizations were carried out by [**15,16]**.

The main features of these configurations are mentioned below since they are necessary to correctly impose the phenomena as a boundary condition.

- Quiescent: The swirl angle pattern is characterised by its unsteadiness which stems from the complexity of the flow field, as the flow coming from far downstream interacts with the one travelling from far upstream. Initially, two counter-rotating vortices are observed. However, as the time passes by a single vortex becomes dominant as illustrated in Figure 5. Beyond this point, the flow gets locked in this mode.
- Headwind: Two counter-rotating vortices of a higher strength than the previous ones are characteristic of this configuration. Fig. 5 shows how the flow field changes as the velocity ratio does and the particular direction of rotation of each mode.
- Crosswind: The strength of the ground vortex formed when the wind has a certain tangential velocity component may be three times higher than in the case of headwind. Furthermore, lip separation accompanies the vortex formation increasing the level of flow distortion. Nonetheless, the level of total pressure drop inside the vortex is more severe than the one associated with the flow separation. The most hazardous case is represented by a pure crosswind, namely, a yaw angle of 90 degrees. The latter value was the one used in this study.
- Take-off and thrust reverse operation: The effect of a moving intake was observed by **[15]**, via the use of a moving ground and a static intake. In relation to the swirl

angle distribution, two counter-rotating vortices were consistently reported with a lower strength than in the case of headwind condition. The aircraft tests carried out by **[16,17,18]** enabled depiction of the flow field features. Again, two vortices were found to be ingested by the engine. In fact, thrust reversal can be seen as the opposite case to take-off. The deceleration of the aircraft and the reverse flow jets create a particularly strong tailwind which acts as the source of vorticity. Although values of circulation were not reported, the levels of total pressure drop can be compared to the ones provided by **[15]**. Therefore, circulation values can be inferred to be slightly higher than in the case of headwind, which may be due to the considerable level of tailwind during the deceleration of the aircraft.

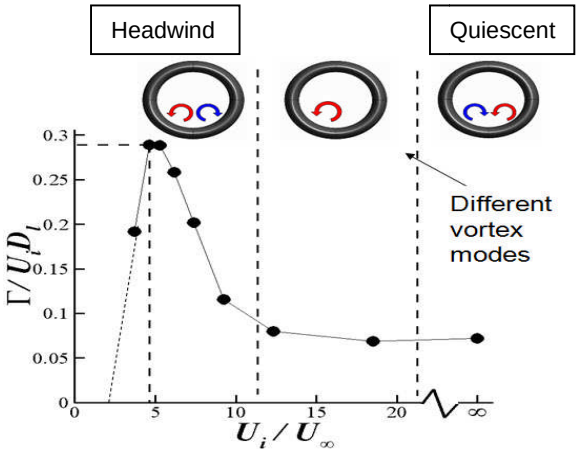

Figure 5. Transition from quiescent to headwind conditions showing the vortex pattern [15].

As aforementioned, the inputs to calculate the vortex strength are the non-dimensional velocity ratio and the non-dimensional intake height. The latter parameter can be easily fixed if one considers current wing-mounted subsonic intakes. The values selected were 0.3, 0.4 and 0.5, since a considerable spectrum of bypass ratios are covered by these values. The problem arises from the fact of not having a specified dimensionless velocity and thus, a methodology had to be developed. By selecting the design point within the speedline, a value of mass flow is therefore fixed. Knowing the mass flow and the area of the intake, the velocity at the entry of this can be calculated via mass flow continuity. This allows varying the wind velocity and therefore, the velocity ratio, obtaining curves of circulation against velocity ratio for the three different clearances from the ground. The layout of the methodology can be summarized in a flow chart as shown in Figure 6. The question now is which point to select. The most demanding situation which corresponds to the point of maximum circulation was chosen to be simulated. In this way, for each non-dimensional height a value of wind velocity has been fixed such that the circulation is maximum. However, for the rest of the points within the speedline the wind velocity has not been determined yet. For this purpose, it was assumed that a constant value of wind velocity should be used. The reasoning is based on the fact that the wind velocity remains roughly constant when the aircraft is on the ground, but not the throttling which can vary from choking to stalling conditions. Hence, once the wind velocity is known, the circulation for the whole range of mass flows is calculated.

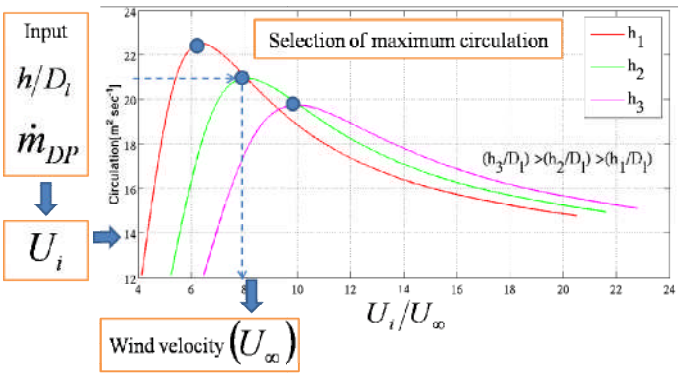

Figure 6. Flow diagram depicting the procedure to calculate the circulation for a complete speedline.

To point out, it has assumed a typical value of the diffusion factor along the intake and that there is no effect of the intake on the vortex pattern or strength. However, **[l9]** demonstrated that this may not be the case for every scenario.

The application of the explained procedure using the specifications of the two rotor geometries in terms of mass flow and annulus diameter permits calculation of circulation for all the points within the speedline. This results in what the author names the “circulation compressor maps”, which are basically compressor characteristics relating circulation and mass flow for each speedline. The reader should think about these maps as the classic compressor maps but substituting the variable in the vertical axis by the vortex strength. An example for the case of Rotor 67 in a crosswind configuration is presented in Fig.7.

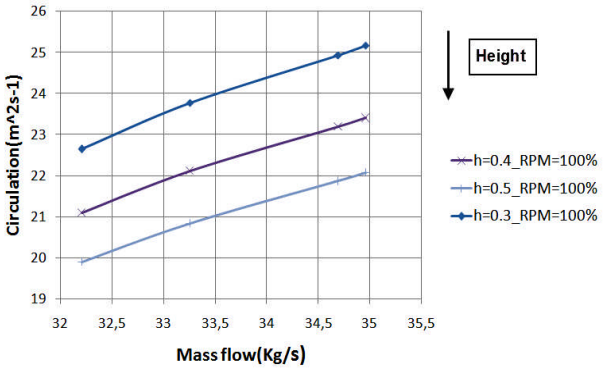

Figure 7. Circulation fan map particular of a crosswind configuration: Rotor 67.

To find the analytical expression of these curves, one just has to fit a polynomial. In this way, the relationship between the circulation and mass flow becomes known. At this point, it should be pointed out again that the boundary condition at the exit of the domain is a value of static pressure. Thus, the value of mass flow is not known a priori, and likewise, the circulation. A solution for this problem would be to impose the expressions found for the circulation vs. mass flow curves, as a dynamic re-reading boundary condition. In this way, in each time step the value of the mass flow is calculated altering the value of the vortex circulation. However, such approach is restricted to unsteady simulations where a real time step can be defined. Therefore, the solution adopted was to impose the maximum value of circulation at design point for all the points within the speedline. To a certain sense, this approach is more consistent with the SAE Standard **[2]**, where the swirl pattern remains the same for all the points within the speedline. Furthermore, the convergence of a simulation where the inlet boundary condition is permanently changing up to a point where the solution does not change further may be very expensive in terms of computational resources.

However, apart from the vortex circulation, the swirl distribution has to be ascertained. For this purpose, ground vortices have been identified to fit well with known vortex models such as the Vatistas' vortex model. Eq. (6-7) present the mathematical expressions of the vortex flow field. Notice that the radial velocity (Eq.7) is multiplied by the kinematic viscosity of the air and thus, it is usually neglected **[14].** Two other parameters were specified: the vortex core radius which is consistently found to be about 6% of the intake diameter and the shape factor (n) equal to one. These are typical values for the ground vortex case used by other researchers **[15]**.

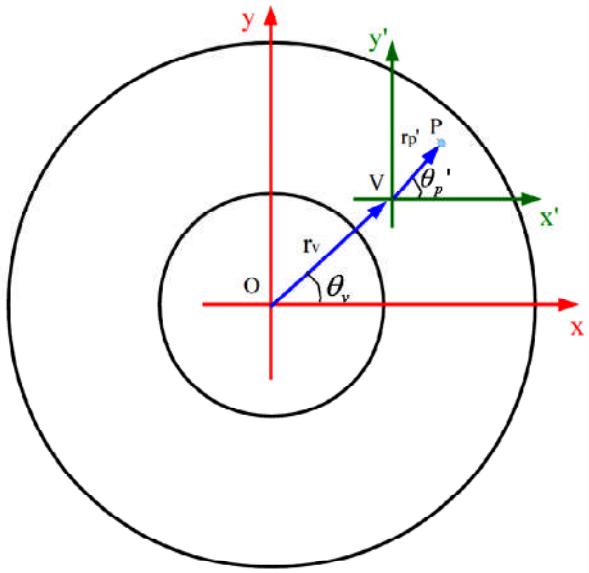

Figure 8. Depiction of the change of coordinates.

$$V_{\theta,p}{}' = \left(\frac{\Gamma}{2\pi r_c}\right)\left(\frac{\frac{r_p{}'}{r_c}}{\left(1+\left(\frac{r_p{}'}{r_c}\right)^{2n}\right)^{1/n}}\right) \tag{6}$$

$$V_{r,p}{}' = \left(\frac{v}{r_c}\right)\left(\frac{2(1+n)\left(\frac{r_p{}'}{r_c}\right)^{2n-1}}{1+\left(\frac{r_p{}'}{r_c}\right)^{2n}}\right) \tag{7}$$

Referring to Fig.8, Eq.(6) is defined on a local coordinate system with origin coincident on the vortex centre (V). However, in order to generalize the expression for any vortex location, it is desirable to define it on a global coordinate system with origin at the centre of inlet face (O). The change of coordinate system involves transferring the definition of velocity components from *(x',y')* to *(x,y)*. The new formulae for the vortex flow field can be observed in Eq. (8-10), which split ($V_{\theta,p}$') into velocity components into the global coordinate system. However, the loss of surge pressure ratio of LP compressors and fans due to radial velocity component (Eq.(10)) is small and therefore its effect is neglected **[24].**

$$\begin{aligned} r_p{}' &= \sqrt{r^2 + r_v^2 - 2\cdot r_p \cdot r_v \cdot \cos\left(\theta_p - \theta_v\right)} \\ x_p{}' &= r_p\cos\theta_p - r_v\cos\theta_v \\ y_p{}' &= r_p\sin\theta_p - r_v\sin\theta_v \\ \theta_p{}' &= a\tan\left(\frac{y_p{}'}{x_p{}'}\right) \end{aligned} \tag{8}$$

$$V_{\theta,p} = \left(\frac{\Gamma}{2\pi r_c}\right)\frac{r_p{}'}{r_c}\left(\frac{1}{1+\left(\frac{r_p{}'}{r_c}\right)^2}\right)\cdot\left(\sin\theta_p{}'\sin\theta_p + \cos\theta_p{}'\cos\theta_p\right) \tag{9}$$

$$V_{r,p} = \left(\frac{\Gamma}{2\pi r_c}\right)\frac{r_p'}{r_c}\left(\frac{1}{1+\left(\frac{r_p'}{r_c}\right)^2}\right)\cdot\left(\cos\theta_p'\sin\theta_p - \sin\theta_p'\cos\theta_p\right) \quad (10)$$

Knowing the expression for the circumferential velocity on local coordinate system, the cosine directors can be calculated as it was done for the case of bulk swirl. A snapshot reflecting how the circumferential velocity (V_θ) components looks like in CFX at inlet domain is presented in Fig. 9.

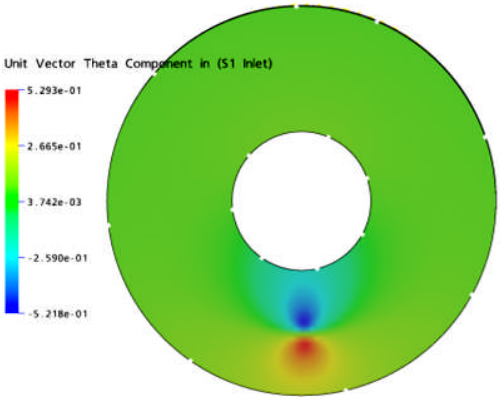

Figure 9. Inlet boundary condition: Crosswind configuration-1 vortex

VALIDATION STUDY

Rotor 37

The mesh sensitivity analysis is presented in Fig. 10 which also includes the experimental speedline. Focusing first on the cases without tip clearance, as expected the pressure ratio is overestimated which is likely to be due to a higher strength of the shock wave simulated. As it was suggested earlier, a solution could have been to decrease the value of y^+ since this reduces the boundary layer thickness and therefore, the recirculation within it. However, it can be observed that the effect of altering the dimensionless wall distance is nearly negligible. In terms of increasing the number of nodes, the fine mesh tends to be more in agreement with the experimental data, whereas the coarse mesh seems to better predict the pressure ratio at near stalling conditions. This result may be due to a possible smearing of the shock wave and hence, not capturing its real strength.The under prediction of the efficiency was already expected as the CFD results should be increased by a 2% in order to be comparable with the experimental data **[11]**. Therefore, observing for example the medium mesh, the greatest relative error is 1.7% which is in accordance with the last assertion. To note that the poor performance of the hi-fi mesh agrees with the underestimation already obtained using a K-omega model by **[20]**. For the meshes with a modelled tip clearance, the choking mass flow is closer to the experimental one than in the case of not modelling the tip gap. In fact, the higher mass flow blockage characteristic of the former cases may be the reason why the choking mass flow value has a lower error.

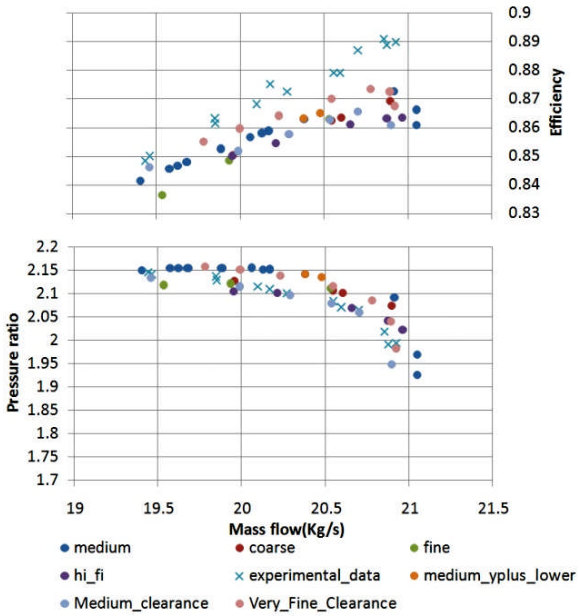

Figure 10. Mesh sensitivity study: Efficiency map and Compressor pressure ratio map

Other comparison which can be carried out in order to validate the CFD results is the span distribution of total pressure and total temperature ratio at the near-stall point. In Fig. 11 appears a comparison between the medium mesh, the experimental data and the results from previous researchers. From the distribution of pressure ratio, it can be observed that the deficit of pressure ratio at 20% of the span from the hub has been captured. As **[21]** verified, this low pressure region seems to be caused by a hub corner stall.

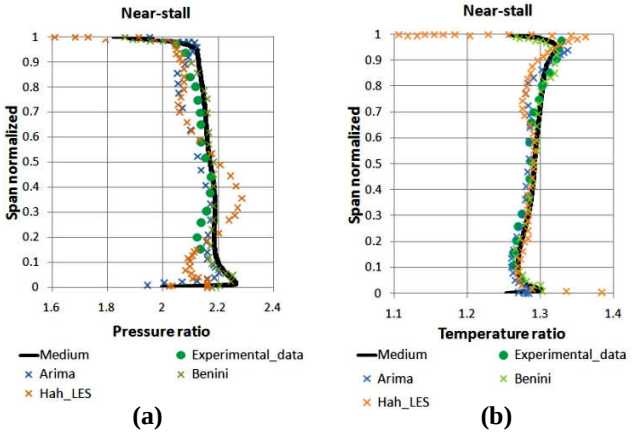

Figure 11. Validation study a) Span distribution of pressure ratio b) Span distribution of temperature ratio [8,20]

Rotor 67

As for the case of Rotor 37, mesh sensitivity was carried out for Rotor 67. The values of pressure ratio and efficiency are in general terms in agreement with the experimental data. In fact, the level of total pressure ratio is nearly the same as in the test cascade. Nonetheless, the same cannot be said about the mass flow. It can be noticed that there is a certain shift to the left in the simulated characteristic. The relative error of the calculated choking mass flow is of 1.15%. Note that to change the total pressure profile at the inlet augmenting or reducing the boundary layer thickness has an effect on the mass flow. Therefore, the imposition of a constant value and the extension of the inlet block may have led to the lower flow coefficient. Moreover, the measurements error should also be considered. In terms of the different meshes, it seems that there is not a significant change between them. Nevertheless for this rotor geometry, the hi-fi mesh (K-omega SST model) performance is fairly good. However, the difference between such a computationally demanding mesh and for example, the medium mesh, is nearly negligible. Again, cases with a lower y^+ were run, although the results were not so distinct in comparison to the case with the higher dimensionless wall distance.

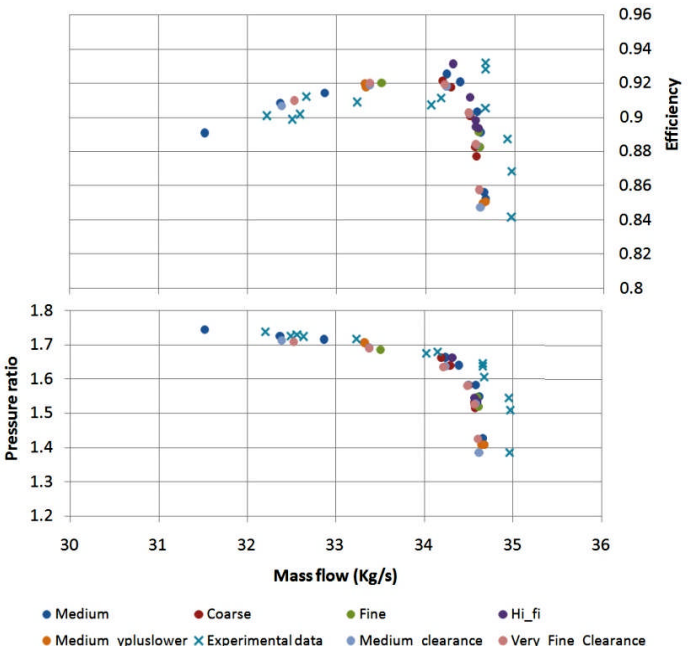

Figure 12. Mesh sensitivity study: Efficiency map and Compressor pressure ratio map

Span distributions

In this case, the span distributions of the total pressure and total temperature ratio at the near-peak efficiency point are presented in Fig.13. The agreement with the experimental data, particularly the total pressure ratio is well within the error range. Nonetheless, the total temperature ratio seems to be over predicted beyond 30% of the span which can be related to the lower estimated efficiency in comparison to the maximum experimental value. Although not being as well-known as in the case of Rotor 37, a low pressure deficit region around 40% of the span was slightly detected. This is quite encouraging as this flow feature represents a challenge for the CFD solver.

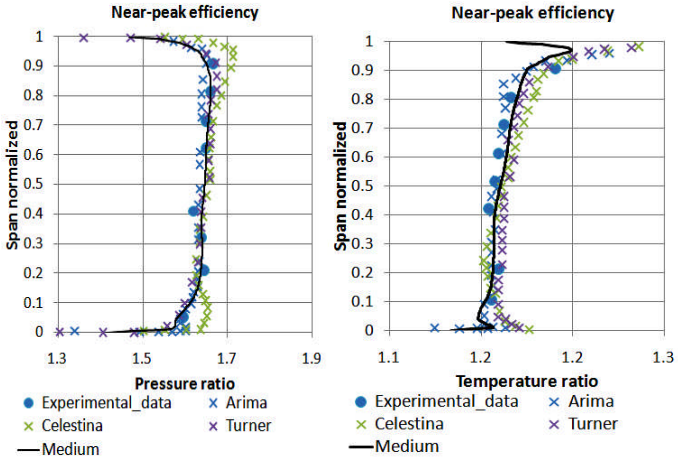

(a) **(b)**

Figure 13. Validation study a) Span distribution of pressure ratio b) Span distribution of temperature ratio [8,13]

The outcome of the mesh sensitivity was the selection of a mesh for the full-annulus simulations. As stated before, the medium mesh was selected. The main two reasons are the following. Firstly, there is a limitation in the number of nodes which could be simulated. This also explains why the tip clearance was not modelled for the full-annulus case; since if nodes are delegated to capture the complex tip clearance flow, the rest of the span is modelled with a lower accuracy. Secondly, the agreement with the experimental data is within the test cascade error range. Moreover, the aim of the simulations is to calculate deltas of loss in stability pressure ratio for the clean and the distorted case by means of simulating the same mesh.

BULK SWIRL

Rotor 67

One of the favourable characteristics of bulk swirl regarding CFD simulations is the axisymmetry of the flow. Thus, one-flow passage simulations are capable of capturing the effect of imposing an absolute flow angle at the inlet. In terms of boundary conditions, the fan was subjected to positive and negative swirl content as the complexity of the problem does preclude some type of possible symmetry of the problem. The magnitude of the swirl was chosen to be 5 degrees. Observing Fig.14, the shift of the speedlines is in agreement with the results obtained by **[28].** The explanation of the shape of the new speedlines can be based on the change of the velocity diagrams. In fact, the total pressure ratio is given by

the combination of mass flow and incidence. For the case of co-rotating swirl, the compression system handles the decrease in incidence by means of reducing the mass flow and hence, the height of the inlet velocity triangle. However, the effect of a falling incidence is dominant and the pressure ratio diminishes; this explains the shift to the left and downwards. The case of counter-rotating swirls is the opposite; the increase in incidence is coped by increasing the mass flow. The latter rises the value of the choking mass flow and displaces the speedline to the right and upwards. In terms of isentropic efficiency, the effect of a co-rotating swirl results in an increase of efficiency below a particular corrected mass flow. This is again associated with the previous explanation. The decrease of total pressure ratio is also accompanied by a drop in total temperature ratio, as the distance between the peaks of the velocity triangles is shortened. The rise of efficiency may be due to a greater drop of temperature ratio in comparison with the decrease in pressure ratio. Of course, these arguments lie in the fact of a nearly constant velocity triangle at the rotor exit. Although this is not totally true, it allows envisaging of compressor map tendencies.

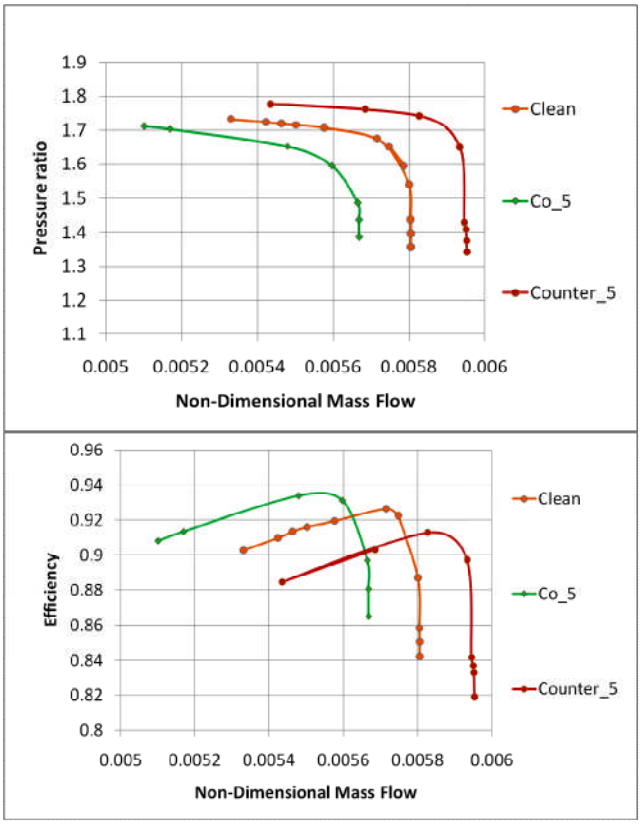

Figure 14. Rotor 67: Compressor maps when subject to pure bulk swirl

Rotor 37

Since the main comments concerning the effect of bulk swirl on turbomachinery have already been highlighted, this section is only aimed to differentiate between the results from Rotor 67 and 37. The movement of the speedlines is again in accordance with the previous explanation given. Note that, particularly for this case, the changes in mass flow tends to be counterbalanced by the changes in incidence as the stalling condition is reached. This can be seen in Fig.15, where the value of the total pressure ratio is roughly the same for the three swirl contents plotted. Moreover, the higher efficiency characteristic of the co-rotating swirl can be easily observed in the efficiency map. For Rotor 37, this tendency is more observable due to the slope of the efficiency curve which is primarily positively sloped.

All in all, the gain in stability pressure ratio when a negative swirl is acting at the inlet is lower than the loss related to a positive swirl content for the case of Rotor 37. Although the previous assertion may sound confusing, please note that the loss in stability pressure ratio is defined in terms of pressure ratio and not in terms of corrected airflow. However, this is also associated to the fact of having simulated only the design speedline.

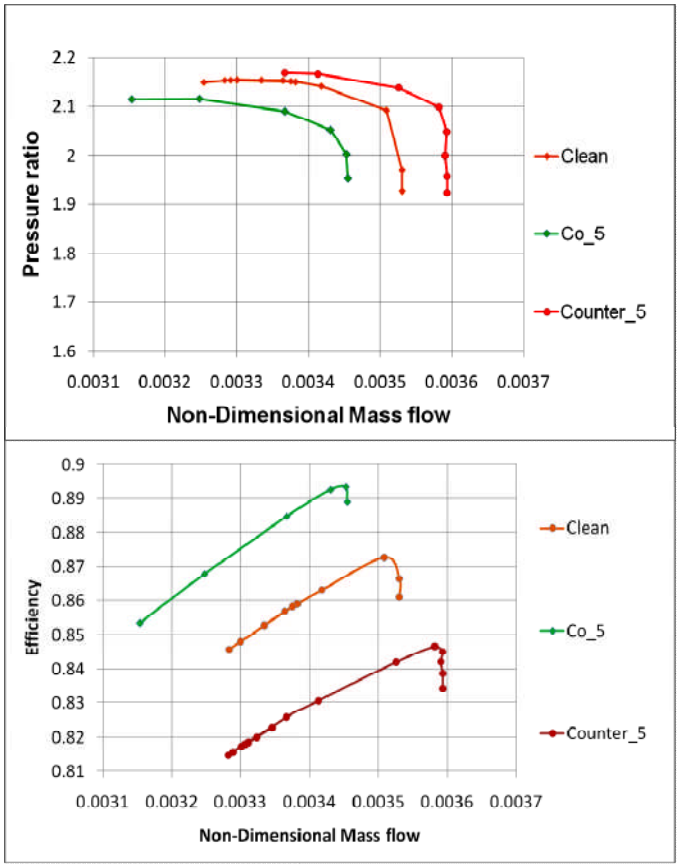

Figure 15. Rotor 37: Compressor maps when subject to pure bulk swirl

GROUND VORTEX INGESTION

NASA Rotor 67 was chosen for this type of swirl distortion case as it is a fan geometry, where ground vortex may only occur. Particularly for this study, the vortex core was located at three different radial positions but consisting same vortex strength. The vortex was defined as counter-rotating when located at the hub and shroud, whereas it was co-rotating when positioned at the mid-span position as shown in Fig.16.

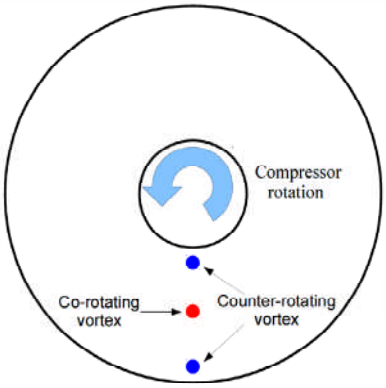

Figure 16. Depiction of the parametric radial position study

Despite the fact of having included the three distorted speedlines within the same chart, the comments with regards to each case is added separately. This is intended to facilitate the understanding of the completely different behaviour of the fan when the radial position of the vortex core is varied.

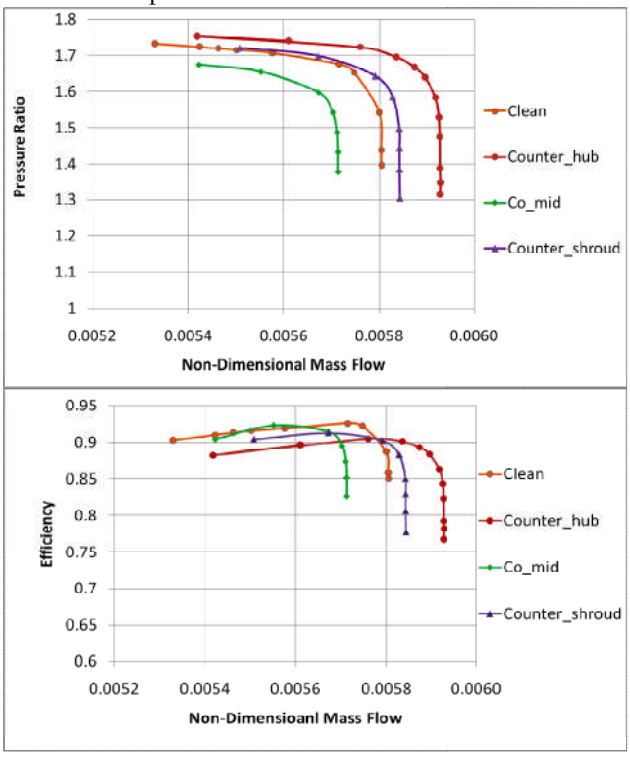

Figure 17. Rotor 67 compressor maps when subject to ground vortex in a crosswind configuration

1. Hub

Observing Fig.17, the speedline has been shifted to the right and upwards, namely, higher mass flow and pressure ratio. This is characteristic of a counter-rotating swirl since the majority of the blade span is exposed to a negative swirl content. In terms of efficiency, the explanation presented for the case of pure bulk swirl is totally applicable to this case. Note that although the majority of the span experiences an increase of the incidence, the aerodynamic loading at the hub is reduced. If one considers a free vortex design of the rotor, the reduction of the loading at the hub allows extending the stability range of the compressor. However, transonic fans are usually characterised by stalling at the tip region due to the interaction between the shock wave and the tip leakage vortex. The reader is reminded that the full-annulus mesh did not fit tip clearance due to computational resources. Therefore, the effect of stabilizing the hub becomes dominant and this may be the reason why the stalling point is reached at a slightly lower mass flow.

2. Midspan

The midspan position is a particularly interesting case since half of the blade is subject to a positive swirl and the other half to a negative swirl. In this case, a co-rotating vortex was chosen to be simulated because it enables to highlight the differences with respect to the counter-rotating case. A question which stems from such distribution is that of which half becomes dominant.

The answer is implicit in the fan map. The movement of the speedline towards a lower mass flow and pressure ratio implies that the co-rotating bulk swirl dominates. Although the throttling of the hub provokes an increase in axial velocity and hence, a rise of mass flow. However, the extent of positive swirl content dominates as it was expected. In spite of presenting a pressure ratio map characteristic of a co-rotating swirl, it is not so easy to attribute such behaviour to the efficiency map. Even though the mass flow has decreased, the efficiency is only slightly greater than in the clean case. This effect is associated with another half of the blades which is subjected to a counter-rotating swirl and thus, a higher temperature ratio leading to the drop of efficiency. To locate the vortex core at the mean radius allows the swirl distribution being developed more correctly than at the hub or at shroud.

3. Shroud

The speedline corresponding to the simulation where the vortex is imposed at 75% of the span is the one closest to the clean speedline. In this case, the majority of the blade undergoes a co-rotating swirl which reduces the incidence. However, the tip region operates with an increased relative angle. All this causes the shift of the speedline towards the right-hand side of the map and increasing slightly the level of pressure ratio. The movement to higher mass flows may be due to the increase of the height of the velocity triangles at the shroud. In fact, in this region the relative angle is the greatest due to high rotational speed. This implies that the fan in order

to cope with the flow angularity sucks more airflow in the upper part of the blade in an effort to reduce the incidence.

CONCLUSIONS

A comprehensive investigation of the development of boundary conditions to model inlet flow distortion as an inlet boundary condition for CFD simulations regarding turbomachinery flows has been presented. Particular emphasis has been given to the swirl distortion problem due to the importance it has gained recently. To accomplish such a challenging task, several steps were carried out before simulations could be carried out. The geometry and mesh generation of two transonic compression systems were created. Rotor 37 and 67 were selected due to the extensive available data in the public domain. The following step involved a grid dependency study varying not only the number of nodes but also the turbulence model, the dimensionless wall distance and the tip clearance region modelling. The tip clearance effects were considered negligible for steady simulations as main objective of this work was not to run unsteady simulations and predict rotating stall accurately but to analyze the global performance of a transonic rotor, when simulated under two types of swirl distortion. In addition, a comparison against experimental data demonstrated the quality of the developed CFD capability. Once the latter study was finished, a mesh for the distorted cases was chosen. As distorted boundary conditions, three different cases were considered. With reference to inlet swirl distortion, the most simple and the most complex cases were developed, pure bulk swirl and ground vortex ingestion respectively. Furthermore, a method to calculate the circulation of ground vortices was implemented. This permitted to carry out a parametric study, varying the ground clearance, the vortex mechanism and even the vortex radial location. The latter was done in an effort to emphasize the different effect of defining the vortex core at the hub, midspan or shroud but keeping the vortex strength constant.

The results of the distorted simulations allowed identification of the effect of flow angularity on turbomachinery. The shift arising as a consequence of the presence of bulk swirl was related to the change that velocity diagrams undergo. The understanding of these simple cases permitted to ascertain the impact of ground vortices. In fact, three different vortex radial positions were simulated in an effort to highlight the importance of the vortex core location. The shift of the three speedlines with respect to the clean condition is in accordance with what was observed in the bulk swirl cases.

ACKNOWLEDGMENTS

The authors would like to express their gratitude to Richard Tunstall, Barry Moore and Gordon Warnes from Rolls-Royce plc for their support to this project. Thanks also to Dr. Joao Amaral Teixeira for his advice during the development of the numerical model.

REFERENCES

[1] S16 Turbine Engine Inlet Distortion Committee (1983),"Inlet Total-Pressure-Distortion Considerations for Gas-Turbine Engines", Society of Automotive Engineers, AIR5686, p. 1-280.

[2] S16 Turbine Engine Inlet Distortion Committee (2007),"A methodology for Assessing Inlet Swirl Distortion", Society *of Automotive Engineers*, AIR5686, p.1-108.

[3] Williams, D. (2010), *Airframe engine integration*, Cranfield University, Propulsion systems performance and integration lecture notes.

[4] Reid, L., Moore, R. D., (1978), *Design and overall performance of four highly loaded, high-speed inlet stages for an advanced high-pressure-ratio core compressor*, Lewis Research Center, Nasa technical paper 1337, p. 1-132.

[5] AGARD Propulsion and Energetics Panel Working Group 26, (1998),"CFD validation for propulsion system components", AGARD advisory report, Vol. AR-355, p. 1-100.

[6] Strazisar, A. J., Wood, J. R., Hathaway, M. D., Suder, K. L. (1989), *Laser anemometer measurements in a transonic axial-flow fan rotor*, Lewis Research Center, Nasa technical paper 2879, p. 1-220.

[7] Niazi, S. (2000), *Numerical simulations of rotating stall and surge alleviation in axial compressor*, "Georgia Institute of Technology", PhD Thesis.

[8] Arima, T., Sonoda, T., Shirotori, M., Tamura, A., Kikuchi, K. (1999),"A numerical investigation of transonic axial compressor rotor flow using a low-Reynolds-Number k-epsilon turbulence model", Journal *of Turbomachinery*, Vol. 121, p.44-58.

[9] Longley, J.P., Greitzer, E.M. (1992),"Inlet distortion effects in aircraft propulsion system integration", *AGARD Lecture Series*, Vol. 183(6), p. 1-17.

[10] Tu, J., Yeoh G.H., Liu, C. (2008),"Computational Fluid Dynamics - A practical Approach", BH, Oxford.

[11] Denton, J.D. (1996),"Lessons from Rotor 37", *Journal of Thermal Science*, Vol.6 (1), p. 1-12.

[12] Chima, R. V. (1996),"Calculation of tip clearance effects in a transonic compressor rotor", in *41st Gas Turbine and Aeroengine Congress*, NASA TM 107216, June 1996 Birmingham, p. 1-11.

[13] Jennions, I. K., Turner, M. G. (1993),"Three-dimensional Navier-Stokes computations of transonic fan flow using an

explicit flow solver and an implicit k-epsilon solver", *Journal of Turbomachinery*, Vol. 115, p. 261-272.

[14] Johns, C. (2002),"The aircraft engine inlet vortex problem", in *AIAA's Aircraft technology, integration and operations (ATIO)*, AIAA-2002-5894, October 2002 California, p. 1-13.

[15] Murphy, J. (2008), *Intake ground vortex aerodynamics*, Cranfield University, PhD Thesis.

[16] Brix, S., Neuwerth, G., Jacob, D. (2000), "The inlet vortex system of jet engines operating near the ground", *American Institute of Aeronautics and Astronautics*, AIAA-2000-3998, p. 75-85.

[16] Motycka, D. L., Walter, W. A. (1976), "An experimental investigation of ground vortex formation during reverse operation", in 11th American Institute of Aeronautics and Astronautics and Society of Automotive Engineers, Propulsion Conference, AIAA-1975-1322, October 1975 California, p. 1-4.

[17] Motycka, D. L., Walter, W. A., Muller, G. L. (1973), "An analytical and experimental study of inlet ground vortices", *in 9th American Institute of Aeronautics and Astronautics and Society of Automotive Engineers, Propulsion Conference*, AIAA-1973-1313, November 1973 Las Vegas, p. 1-8.

[18] Motycka, D. L. (1975), "Ground vortex-limit to engine/Reverser operation", American society of automotive engineers, 75-GT-3.

[19] Mitchell, G.,(1975), *Effect of inlet ingestion of a wing tip vortex on compressor face flow and turbojet stall margin*, Lewis Research Centre, NASA TM X-3246, p. 1-78.

[20] Biollo, R., Benini, E. (2009),"Shock/Boundary-Layer/Tip-clearance interaction in a transonic rotor", *Journal of Propulsion and Power 2009*, Vol. 25(3), p. 668-677.

[21] Hall, C. (2009), *Large eddy simulation of transonic flowfield in NASA Rotor 37*, Glenn Research Center, NASA TM 2009-215627, p. 1-18.

[22] Adamczyck, J. J., Celestina, M. L., Greitzer, E. M. (1993),"The role of tip clearance in high-speed fan stall", *Journal of Turbomachinery*, Vol. 115, p. 28-39.

[23] Pintat, L. (2006), *High-fidelity aerodynamic optimization of a transonic fan rotor*, "Cranfeld University", MSc Thesis.

[24] R.G.Hercock., *Effect of intake flow distortion on engine stability*, "Installation Aerodynamics Group, Rolls-Royce Plc".

[25] Sheoran, Y., Davis, M., Beale, D. (2008), "Integrated test and evaluation techniques as applied to an inlet swirl investigation using the F109 gas turbine engine", in *Proceedings of ASME Turbo Expo 2008: Power for Land, Sea and Air*, GT2008-50074, June 2008, p. 9

